

Inverse problem for the Helmholtz equation with Cauchy data: reconstruction with conditional well-posedness driven iterative regularization

Giovanni Alessandrini* Maarten V. de Hoop† Florian Faucher‡
 Romina Gaburro§ Eva Sincich*

May 8, 2022

Abstract

In this paper, we study the performance of Full Waveform Inversion (FWI) from time-harmonic Cauchy data via conditional well-posedness driven iterative regularization. The Cauchy data can be obtained with dual sensors measuring the pressure and the normal velocity. We define a novel misfit functional which, adapted to the Cauchy data, allows the independent location of experimental and computational sources. The conditional well-posedness is obtained for a hierarchy of subspaces in which the inverse problem with partial data is Lipschitz stable. Here, these subspaces yield piecewise linear representations of the wave speed on given domain partitions. Domain partitions can be adaptively obtained through segmentation of the gradient. The domain partitions can be taken as a coarsening of an unstructured tetrahedral mesh associated with a finite element discretization of the Helmholtz equation. We illustrate the effectiveness of the iterative regularization through computational experiments with data in dimension three. In comparison with earlier work, the Cauchy data do not suffer from eigenfrequencies in the configurations.

1 Introduction

Iterative methods for the recovery of subsurface parameters have been collectively referred to, in reflection seismology, as Full Waveform Inversion (FWI). FWI consists in the minimization of the residuals, defined as some difference between the observed and modelled data. FWI was originally formulated with time-domain data using an energy norm in the misfit functional by Lailly [18] and Tarantola [31, 32]. The time-harmonic formulation of the seismic inverse problem was later considered by Pratt *et al.* [26, 25]. Standardly, one applies the adjoint state method for the implementation of the minimization procedure.

To mitigate the nonlinearity and ill-posedness of the inverse problem, hierarchical multiscale strategies have been developed. In the time-domain, Bunks *et al.* [10] proposed successive inversion of data subsets of increasing frequency contents. This multiscale approach can be related to the subspace search method introduced in [17]. Multiscale Gauss-Newton-Krylov methods were developed by Akcelik *et al.* [2] and many further developments have taken place since then. The application of wavelet bases enabling successive levels of model compression were considered by Loris *et al.* [22, 21] in wave-equation tomography and in FWI by Lin *et al.* in [20], Yuan and Simons in [36, 37]. These ideas were natural but lacked foundation and understanding of convergence. In [15], the authors developed

*Dipartimento di Matematica e Geoscienze, Università di Trieste, Italy.

†Department of Computational and Applied Mathematics and Department of Earth Science, Rice University, Houston TX 77005, USA.

‡Project-Team Magique-3D, Inria Bordeaux Sud-Ouest Research Center, Laboratoire de Mathématiques et de leurs Applications, Université de Pau et des Pays de l'Adour, CNR, France.

§Department of Mathematics and Statistics, Health Research Institute (HRI), University of Limerick, Limerick, Ireland.

an iterative regularization approach with a multilevel strategy derived from conditional Lipschitz stability estimates with a convergence analysis. For the regularization they introduced a multiscale hierarchy of subspaces for which the Lipschitz stability estimates hold, with an associated model compression rate through projections. This compression rate appears in the convergence analysis and mitigates the growth of stability constants with scale refinement, that is, increasing dimension of the subspaces. In the time-harmonic case, such quantitative stability estimates have been proved for piecewise constant [6] and piecewise linear [3] representations of the wave speed with a given domain partition. Note that, in view of recent work by Cârstea *et al.* [13], on a germane problem in elasticity, it seems quite possible to recover the partition as well, in the case where the domain is composed of sub-analytic sets. In the piecewise constant case, this includes subspaces defined by Haar wavelets, where the analysis in [3] is adapted to general domain partitions such as unstructured tetrahedral meshes, that can be associated with a segmentation. Here, we present a computational framework of our reconstruction algorithm via iterative regularization using piecewise linear representations as stable subspaces, as well as experiments.

We use Cauchy data assimilated from dual sensor acquisition. Cauchy data do not suffer from eigenfrequencies unlike the Dirichlet-to-Neumann map, which, in fact, cannot be observed directly in seismic marine acquisition. For a perspective on dual sensor acquisition devices and simultaneous measurements of pressure and vertical or normal velocity, we refer to [12, 33]. Dual sensor acquisition has additional benefits such as in noise reduction [34, 27]. Independent of earlier analysis, the results presented here confirm the relevance of acquiring dual sensor data. The marine seismic acquisition we consider consists in sources positioned above the fixed receivers lattice. This setup matches the TopSeis acquisition system that has been recently deployed by CGG and Lundin Norway AS¹, for the purpose of improving the near offset data.

The formulation of FWI, and its underlying minimization procedure, has been proposed with norms different from energy norms. Shin and collaborators [30, 5, 29] compared the use of the phase and/or amplitude information in the data. Envelope based misfit functional is considered in [7, 35]. Brossier, Operto and Virieux investigate the use of the L^1 norm in [8], and in combination with L^2 norm in [9]. In this paper, we introduce a new misfit functional which is based upon conditional stability of the inverse problem for Cauchy data. This functional, related to the Green's identity, further allows independent locations for field and computational sources in the discrete settings.

2 Misfit functional and stability result

2.1 Assumptions about the domain Ω

We fix some notations that will be adopted in this paper. Given a point $x \in \mathbb{R}^3$, with $x = (x', x_3)$, where $x' \in \mathbb{R}^2$ and $x_3 \in \mathbb{R}$, $B_r(x), B'_r(x')$ denote the open balls in $\mathbb{R}^3, \mathbb{R}^2$ centred at x, x' respectively with radius r . We also denote by $Q_r(x)$ the cylinder

$$Q_r(x) = B'_r(x') \times (x_3 - r, x_3 + r)$$

and $B_r = B_r(0)$ and $Q_r = Q_r(0)$.

1. We assume that Ω is a domain in \mathbb{R}^3 and that there exist positive constants r_0 and B (r_0 being dimensionally a length, B being an absolute constant), such that

$$(2.1) \quad |\Omega| \leq Br_0^3,$$

where $|\Omega|$ denotes the Lebesgue measure of Ω .

2. We fix an open non-empty subset Σ of $\partial\Omega$ (where the measurements in terms of the local Cauchy data are taken).

- 3.

$$\bar{\Omega} = \bigcup_{j=1}^N \bar{D}_j,$$

¹see <https://www.cgg.com/en/What-We-Do/Offshore/Products-and-Solutions/TopSeis>

where D_j , $j = 1, \dots, N$ are known open sets of \mathbb{R}^3 , satisfying the conditions below.

- (a) D_j , $j = 1, \dots, N$ are connected and pairwise non-overlapping polyhedrons.
- (b) ∂D_j , $j = 1, \dots, N$ are of Lipschitz class with constants r_0 , L see, for example, [1]).
- (c) There exists one region, say D_1 , such that $\partial D_1 \cap \Sigma$ contains a *flat* portion Σ_1 of size r_0 and for every $j \in \{2, \dots, N\}$ there exists $j_1, \dots, j_K \in \{1, \dots, N\}$ such that

$$(2.2) \quad D_{j_1} = D_1, \quad D_{j_K} = D_j.$$

In addition we assume that, for every $k = 1, \dots, K$, $\partial D_{j_k} \cap \partial D_{j_{k-1}}$ contains a *flat* portion Σ_k of size r_0 (here we agree that $D_{j_0} = \mathbb{R}^3 \setminus \Omega$), such that

$$\Sigma_k \subset \Omega, \quad \text{for every } k = 2, \dots, K.$$

We emphasize that under such an assumption, for every $k = 1, \dots, K$, there exists $P_k \in \Sigma_k$ and a rigid transformation of coordinates (depending on k) under which we have $P_k = 0$ and

$$(2.3) \quad \begin{aligned} \Sigma_k \cap Q_{r_0/3} &= \{x \in Q_{r_0/3} \mid x_3 = 0\}, \\ D_{j_k} \cap Q_{r_0/3} &= \{x \in Q_{r_0/3} \mid x_3 > 0\}, \\ D_{j_{k-1}} \cap Q_{r_0/3} &= \{x \in Q_{r_0/3} \mid x_3 < 0\}. \end{aligned}$$

2.2 A-priori information on the wave speed c

We shall consider a real valued function $c \in L^\infty(\Omega)$, with

$$(2.4) \quad 0 < c_{min} \leq c \leq c_{max},$$

for some positive constants c_{min} , c_{max} and of type

$$(2.5a) \quad c(x) = \sum_{j=1}^N c_j(x) \chi_{D_j}(x), \quad x \in \Omega,$$

$$(2.5b) \quad c_j(x) = a_j + A_j \cdot x,$$

where $a_j \in \mathbb{R}$, $A_j \in \mathbb{R}^3$ and D_j , $j = 1, \dots, N$ are the given subdomains introduced in Subsection 2.1.

2.3 Cauchy data and misfit functional

We let Ω denote the subsurface domain with Lipschitz boundary $\partial\Omega$ and Σ the non-empty open portion of $\partial\Omega$ introduced in Subsection 2.1 where the acquisition is carried out. We introduce the subspace of $H^{1/2}(\partial\Omega)$,

$$H_{co}^{1/2}(\Sigma) = \{f \in H^{1/2}(\partial\Omega) \mid \text{supp } f \subset \Sigma\}.$$

Its closure with respect to the $H^{1/2}(\partial\Omega)$ norm is the space $H_{00}^{1/2}(\Sigma)$. In a similar manner, we define $H_{00}^{1/2}(\partial\Omega \setminus \bar{\Sigma})$. We denote the pressure by u . The *Cauchy data* associated to c is the space \mathcal{C}_c^Σ ,

$$\mathcal{C}_c^\Sigma = \left\{ (f, g) \in H^{1/2}(\partial\Omega)|_\Sigma \times H^{-1/2}(\partial\Omega)|_\Sigma \mid \begin{aligned} &\exists u \in H^1(\Omega) \text{ weak solution to } \Delta u + k^2 c^{-2} u = 0 \text{ in } \Omega, \\ &u|_\Sigma = f, \\ &\left\langle \frac{\partial u}{\partial \nu} \Big|_{\partial\Omega}, \varphi \right\rangle = \langle g, \varphi \rangle, \forall \varphi \in H_{00}^{1/2}(\Sigma) \end{aligned} \right\}.$$

Here $\langle \psi, \varphi \rangle$ denotes the duality between the complex valued spaces $H^{-\frac{1}{2}}(\partial\Omega)$, $H^{\frac{1}{2}}(\partial\Omega)$ based on the L^2 inner product

$$\langle \psi, \varphi \rangle = \int_{\partial\Omega} \psi \bar{\varphi}$$

and $H^{\frac{1}{2}}(\partial\Omega)|_{\Sigma}$ and $H^{-\frac{1}{2}}(\partial\Omega)|_{\Sigma}$ denote the *restrictions* of $H^{\frac{1}{2}}(\partial\Omega)$ and $H^{-\frac{1}{2}}(\partial\Omega)$ to Σ respectively. C_c^{Σ} is a subspace of the Hilbert space $H^{\frac{1}{2}}(\partial\Omega)|_{\Sigma} \times H^{-\frac{1}{2}}(\partial\Omega)|_{\Sigma}$.

For the computational experiments we assume that we know the wave speed at the boundary $\partial\Omega$ and we embed Ω in an ambient domain $\Upsilon \supset \Omega$ as we will find convenient to introduce Green's function not precisely for the physical domain Ω but for this augmented domain Υ .

We recall that by assumption 3(c) of Subsection 2.1 we can assume that there exists a point P_1 such that up to a rigid transformation of coordinates we have that $P_1 = 0$ and (2.3) holds with $\Sigma = \Sigma_1$. Denoting by

$$D_0 = \left\{ x \in (\mathbb{R}^3 \setminus \Omega) \cap B_{\frac{r_0}{3}} \mid |x_i| < \frac{r_0}{6}, i = 1, 2; -\frac{r_0}{6} < x_3 < 0 \right\},$$

it turns out that the augmented domain $\Upsilon = \overline{(\Omega \cup D_0)}$ is of Lipschitz class with constants $\frac{r_0}{3}$ and \tilde{L} , where \tilde{L} depends on L only. Given $r > 0$, we set

$$(2.6) \quad \Gamma_1 = \left\{ x \in \Upsilon \mid |x_i| < \frac{r_0}{6}, i = 1, 2; x_3 = -\frac{r_0}{6} \right\},$$

$$(2.7) \quad \Gamma_2 = \partial\Upsilon \setminus \bar{\Gamma}_1,$$

$$(2.8) \quad (\Upsilon)_r = \left\{ x \in \Upsilon \mid \text{dist}(x, \partial\Upsilon) > r \right\}.$$

We also introduce the following sets

$$(2.9) \quad D'_0 = \left\{ x \in D_0 \mid -\frac{r_0}{12} < x_3 < 0 \right\},$$

$$(2.10) \quad D''_0 = \left\{ x \in D_0 \mid -\frac{r_0}{12} < x_3 < -\frac{r_0}{6} \right\},$$

$$(2.11) \quad K_0 = \left\{ x \in D''_0 \mid |x_i| < \frac{r_0}{24}, i = 1, 2; -\frac{13}{96}r_0 < x_3 < -\frac{11}{96}r_0 \right\},$$

$$(2.12) \quad K_1 = \left\{ x \in D''_0 \mid |x_i| < \frac{r_0}{12}, i = 1, 2; -\frac{7}{48}r_0 < x_3 < -\frac{5}{48}r_0 \right\},$$

$$(2.13) \quad \Omega' = \overline{(D'_0 \cup \Omega)}.$$

Note that, fixing the origin at the center of D''_0 , K_0, K_1 are concentric parallelograms scaled by the factors $\frac{1}{4}, \frac{1}{2}$ respectively. Note also that this precise choice of scale parameters is just made for the sake of definiteness. What really matters is the general geometrical configuration, in particular we must have

$$\text{dist}(D''_0, \bar{\Omega}) \geq \frac{r_0}{12} > 0 \quad \text{and} \quad K_0 \subset\subset K_1 \subset\subset D''_0.$$

We shall denote by $\Gamma(x, y)$ the standard fundamental solution to the Laplace equation which is

$$(2.14) \quad \Gamma(x, y) = \frac{1}{4\pi|x-y|}.$$

Definition 1. Let B, N, r_0, L, c_{\min} and c_{\max} be given positive numbers with $N \in \mathbb{N}$. We will refer to this set of numbers as to the *a-priori* data. Several constants depending on the *a-priori* data will appear within the paper. In order to simplify our notation, any quantity denoted by C, C_1, C_2, \dots will be called a constant understanding in most cases that it only depends on the *a-priori* data.

Next we introduce a mixed boundary value problem for $\Delta + k^2c^{-2}$ in Υ which is always well posed, independently of any *a-priori* condition on c , besides the assumption of being real valued and bounded. This shall enable us to construct Green's function for $\Delta + k^2c^{-2}$ in Υ .

We assume that the uppermost part D_0 of the domain Υ represents a region filled by water. The wave speed in D_0 can then be assumed to be known and constant with

$$(2.15) \quad c = c_0, \quad \text{in } D_0.$$

Pressure sources (air gun) are excited to produce impulses located at points in $K_1 \subset D_0$ and Cauchy data are collected through dual sensors located at the surface Σ , which lies below K_1 .

Pressure is assumed to be zero at the sea level Γ_1 (*i.e.*, free surface), and to satisfy, on the remaining part of the boundary Γ_2 (of the region of interest), a (conventional) absorbing condition. If we model this problem in the frequency domain, and assume that the source is modeled by a Dirac's delta concentrated at a point y , the pressure is represented as the Green's function of the following mixed boundary value problem,

$$(2.16) \quad \begin{cases} \Delta G_c(\cdot, y) + k^2c^{-2}(\cdot)G_c(\cdot, y) = -\delta(\cdot - y), & \text{in } \Upsilon, \\ G_c(\cdot, y) = 0, & \text{on } \Gamma_1, \\ \partial_\nu G_c(\cdot, y) - ik_0G_c(\cdot, y) = 0, & \text{on } \Gamma_2. \end{cases}$$

The theory developed, for example, in [11] shows that such a function G_c exists and is unique. Note that the term k_0 is conventionally assumed to be constant and known. The next theorem collects the main features of the Green's function solving (2.16).

Theorem 1. *For any $y \in \Upsilon$, there exists a unique distributional solution $G_c(\cdot, y)$ to (2.16). Moreover, there exists a constant $C > 0$ depending on r_0, L, k and on c_{min} such that for any $x, y \in (\Upsilon)_{r_0}$, $x \neq y$ we have that*

$$(2.17) \quad |G_c(x, y) - \Gamma(x, y)| \leq C$$

and

$$(2.18) \quad |\nabla_y G_c(x, y) - \nabla_y \Gamma(x, y)| \leq C(|\log|x - y|| + 1).$$

Moreover, let Q_{k+1} be a point such that $Q_{k+1} \in B_{\frac{r_0}{8}}(P_{k+1}) \cap \Sigma_{k+1}$ with $k \in \{1, \dots, N-1\}$, then the following inequality holds true for every $x \in B_{\frac{r_0}{16}}(P_{k+1}) \cap D_{j_{k+1}}$ and every $y = Q_{k+1} - re_3$, where $r \in (0, \frac{r_0}{16})$

$$(2.19) \quad |\nabla_y^2(G_c(x, y) - \Gamma(x, y))| \leq Cr^{-1}.$$

Here ∇_y^2 denotes the Hessian matrix.

Proof. Let $y \in \Upsilon$ and let G_0 be the Green's function for the Laplace operator which solves

$$(2.20) \quad \begin{cases} \Delta G_0(\cdot, y) = -\delta(\cdot - y), & \text{in } \Upsilon, \\ G_0(\cdot, y) = 0, & \text{on } \Gamma_1, \\ \partial_\nu G_0(\cdot, y) - ik_0G_0(\cdot, y) = 0, & \text{on } \Gamma_2. \end{cases}$$

The existence and uniqueness of a distributional solution $G_0 \in L^1(\Upsilon)$ to (2.20) is a consequence of standard theory on boundary value problems for the Laplace equation. By standard techniques it can be proved that for any $y \in \Upsilon$ such that $\text{dist}(y, \partial\Upsilon) \geq \frac{r_0}{4}$ we have that $G_0(\cdot, y) \in L^2(\Upsilon)$. Now we define $R_c(\cdot, y) \in H^1(\Upsilon)$ to be the solution to

$$(2.21) \quad \begin{cases} \Delta R_c(\cdot, y) + k^2c^{-2}R_c(\cdot, y) = -k^2c^{-2}G_0(\cdot, y), & \text{in } \Upsilon, \\ R_c(\cdot, y) = 0, & \text{on } \Gamma_1, \\ \partial_\nu R_c(\cdot, y) - ik_0R_c(\cdot, y) = 0, & \text{on } \Gamma_2. \end{cases}$$

The existence and uniqueness for (2.21) follows along the lines of the proof of [3, Proposition 3.1], which relies on the Fredholm alternative theory. Moreover, by arguments based on well-known estimates for the Cauchy problem contained in [3, Proposition 3.1], we have that

$$(2.22) \quad \|R_c(\cdot, y)\|_{H^1(\Upsilon)} \leq C \|G_0(\cdot, y)\|_{L^2(\Upsilon)}$$

and, by standard interior estimates, that

$$(2.23) \quad |R_c(x, y)| \leq C,$$

for any $x \neq y$, $x \in \Upsilon$ and $\text{dist}(y, \partial\Upsilon) \geq \frac{r_0}{4}$. If we form

$$(2.24) \quad G_c(x, y) = G_0(x, y) + R_c(x, y),$$

then we end up with the following estimate

$$(2.25) \quad |G_c(x, y)| \leq C|x - y|^{-1},$$

for any $x, y \in \Upsilon$, $x \neq y$ and $\text{dist}(x, \partial\Upsilon) \geq \frac{r_0}{4}$, $\text{dist}(y, \partial\Upsilon) \geq \frac{r_0}{4}$. The latter combined with the arguments in the proofs of [3, Propositions 3.4, 3.5] suffices to deduce (2.17), (2.18) and (2.19). \square

Assuming that, for sources placed at arbitrary points $z \in K_1$, we can measure associated Cauchy data on Σ :

$$(2.26) \quad G_{obs}(x, z), \quad \frac{\partial}{\partial \nu_x} G_{obs}(x, z), \quad x \in \Sigma,$$

we seek c which minimizes the following misfit functional

$$(2.27) \quad \mathcal{J}(c) = \int_{K_1 \times K_1} \left| \int_{\Sigma} (G_c(x, y) \partial_{\nu} G_{obs}(x, z) - G_{obs}(x, z) \partial_{\nu} G_c(x, y)) d\mu(x) \right|^2 dy dz,$$

where μ denotes the element of surface measure.

The introduction of the misfit functional (2.27) is motivated by the following argument. Given two wave speeds $c^{(i)}$, $i = 1, 2$, consider the Green's functions G_i , introduced in Theorem 1, corresponding to $c^{(i)}$ in Υ and the following quantity

$$(2.28) \quad \mathcal{J}(c^{(1)}, c^{(2)}) = \int_{K_1 \times K_1} |\mathcal{S}_{\mathcal{U}_0}(y, z)|^2 dy dz,$$

where

$$(2.29) \quad \mathcal{S}_{\mathcal{U}_0}(y, z) = \int_{\Sigma_1} (G_1(x, y) \partial_{\nu} G_2(x, z) - G_2(x, z) \partial_{\nu} G_1(x, y)) d\mu(x), \quad \text{for any } y, z \in D_0.$$

It would be a matter of an exercise to show that, fixing $y \in K_1$,

$$(2.30) \quad c \in L^{\infty}(\Upsilon) \rightarrow (G_c(x, y)|_{\Sigma}, \partial_{\nu} G_c(x, y)|_{\Sigma}) \in H^{1/2}(\partial\Omega)|_{\Sigma} \times H^{-1/2}(\partial\Omega)|_{\Sigma}$$

is Fréchet differentiable. Note also that, since we are assuming (2.5a) and (2.5b) (that is, c lives in a finite dimensional space), the $L^{\infty}(\Upsilon)$ norm can equivalently be replaced by the $L^2(\Upsilon)$ norm. This will enable us to apply to \mathcal{J} a projected steepest descent method in Section 3.

Theorem 2. Let Ω , D_j , $j = 1, \dots, N$ and Σ be a domain, N subdomains of Ω and a portion of $\partial\Omega$ as in section 2.1 respectively. Let $c^{(i)}$, $i = 1, 2$ be two wave speeds satisfying (2.4) and of type

$$(2.31) \quad c^{(i)} = \sum_{j=1}^N c_j^{(i)}(x) \chi_{D_j}(x), \quad x \in \Omega,$$

where

$$c_j^{(i)}(x) = a_j^{(i)} + A_j^{(i)} \cdot x,$$

with $a_j^{(i)} \in \mathbb{R}$ and $A_j^{(i)} \in \mathbb{R}^3$, then we have

$$(2.32) \quad \|c^{(1)} - c^{(2)}\|_{L^\infty(\Omega)} \leq C \left(\mathcal{J}(c^{(1)}, c^{(2)}) \right)^{1/2},$$

where C is a positive constant that depends on the a-priori data only.

Remark 1. Note that the introduction of the misfit functional is driven on the one hand by our computational experiments and on the other hand, it is inspired by the method of singular solutions used in previous stability results (see [3] for the case of the Helmholtz equation). Although a natural metric on the space of Cauchy data \mathcal{C}_c^Σ is given by the distance (aperture) d introduced in [3, (2.8)], we have

$$(2.33) \quad \mathcal{J}(c^{(1)}, c^{(2)}) \leq Cd(\mathcal{C}_{c^{(1)}}^\Sigma, \mathcal{C}_{c^{(2)}}^\Sigma)^2$$

and also

$$(2.34) \quad \mathcal{J}(c^{(1)}, c^{(2)}) \leq C \|\Lambda_{c^{(1)}}^\Sigma - \Lambda_{c^{(2)}}^\Sigma\|_*^2,$$

where $\Lambda_c^\Sigma : u \in H^{1/2}(\partial\Omega)|_\Sigma \rightarrow H^{-1/2}(\partial\Omega)|_\Sigma$ is the local Dirichlet-to-Neumann map with its natural norm (here denoted by $\|\cdot\|_*$) between local trace spaces. These estimates justify the use of \mathcal{J} as a substitute to the more traditional quantifications of the error on boundary data (either involving distance of spaces of Cauchy data or boundary maps).

Proof. of Theorem 2.

The proof requires only some adaptations of [3, Theorem 2.2], which are outlined below.

- i) We introduce different boundary conditions. This aspect involves some modifications in the constructions of the Green's function and has been treated in Theorem 1 above. Note that we took advantage of the fact that here we focus on the three-dimensional case only.
- ii) We replace the domain Ω with Ω' and add as initial subdomain D'_0 instead of D_1 . We take advantage of the fact that $c^{(1)} = c^{(2)} = 1$ in $D'_0 \subset \Upsilon \setminus \overline{\Omega}$ which allows us to skip the arguments of [3, Section 4.3].
- iii) We observe that in [3, Theorem 2.2] the right-hand side in (2.20) can be replaced with

$$(2.35) \quad \sup_{K_0 \times K_0} |S_{\mathcal{U}_0}(y, z)|.$$

This follows from the reasoning used in (3.37) of [3, proof of theorem 2.2] with the additional simplification that here $\delta_1 = 0$. Note that the role of \widehat{D}_0 in [3] can be taken with no substantial difference by the set K_0 .

We also recall that $S_{\mathcal{U}_0}(y, z)$ is a solution to

$$(2.36) \quad (\Delta_y + \Delta_z + 2k^2)S_{\mathcal{U}_0}(y, z) = 0$$

in $D_0 \times D_0$ (see [3, (4.61)]). Consequently, by standard estimate of boundedness in the interior we have

$$(2.37) \quad \sup_{K_0 \times K_0} |S_{\mathcal{U}_0}(y, z)|^2 \leq C \int_{K_1 \times K_1} |S_{\mathcal{U}_0}(y, z)|^2 dy dz$$

where $C > 0$ is a constant depending on k and on r_0 .

- iv) Another difference comes from the fact that we are now assuming $c^{(i)}$ piecewise linear instead of $q^{(i)} = k^2(c^{(i)})^{-2}$, for $i = 1, 2$. However due to the assumption (2.4) the estimation of $c^{(i)}, \nabla c^{(i)}$ at each interface is equivalent to that for $q^{(i)}, \nabla q^{(i)}$, for $i = 1, 2$.

□

The stability given in Theorem 2 justifies the use of (2.27) for an optimization algorithm toward the inversion of *Cauchy data to wave speed*.

2.4 Computation of the gradient using the adjoint state method

We start by observing that, although $c \rightarrow G_c(x, y)$ does not map into $H^1(\Upsilon)$ (because of the singularity of the Green's function), the derivative $D_c G_c(x, y)[c]\delta c$ exists and does belong in $H^1(\Upsilon)$. This can be by recalling (2.21) and (2.24). That is

$$(2.38) \quad R_c(x, y) = G_c(x, y) - G_0(x, y) \in H^1(\Upsilon),$$

and the second term G_0 is independent of c . Hence we may well define

$$(2.39) \quad D_c G_c(x, y)[c]\delta c = D_c R_c(x, y)[c]\delta c.$$

We denote

$$(2.40) \quad H_{\Gamma_1}^1(\Upsilon) = \{v \in H^1(\Upsilon) \mid v|_{\Gamma_1} = 0\}.$$

We continue with the variational formulation of Problem (2.16). As noted above, denoting $R_c(x, y) = G_c(x, y) - G_0(x, y)$, it can be formulated as

$$(2.41) \quad \int_{\Upsilon} k^2 c^{-2}(x) G_c(x, y) v(x) - \nabla_x R_c(x, y) \cdot \nabla_x v(x) dx + \int_{\Gamma_2} ik_0 R_c(x, y) v(x) d\mu(x) = 0,$$

for every $v \in H_{\Gamma_1}^1(\Upsilon)$.

The parameter reconstruction is conducted via an iterative minimization of the misfit functional \mathcal{J} of (2.27), in a gradient descent algorithm. Therefore, we require the computation of the gradient of \mathcal{J} . For this purpose, we employ the adjoint state method, which allows the computation of the gradient without having to form explicitly the derivative G'_c . The method arose from the work of [19] and was promoted in the context of parameter derivation in [14]. It has massively been employed since then, and we refer to [24] for a review in the geophysical framework.

We first postpone the sum over the sources in the misfit functional (2.27), and select a single source for G_c and G_{obs} , y and z respectively. We introduce

$$(2.42) \quad \mathcal{I}(c)(y, z) = \left| \int_{\Sigma} \left(G_c(x, y) \partial_\nu G_{obs}(x, z) - G_{obs}(x, z) \partial_\nu G_c(x, y) \right) d\mu(x) \right|^2 = |S_{\mathcal{U}_0}(y, z)|^2,$$

such that

$$(2.43) \quad \mathcal{J}(c) = \int_{K_1 \times K_1} \mathcal{I}(c)(y, z) dy dz.$$

The Riesz representation theorem gives

$$(2.44) \quad D_c \mathcal{I}[c]\delta c = \int_{\Upsilon} \nabla_c \mathcal{I} \delta c dx,$$

where $\nabla_c \mathcal{I}$ is the gradient, and $D_c \mathcal{I}$ is the differential defined for every $\delta c \in L^2(\Upsilon)$ by

$$(2.45) \quad D_c \mathcal{I}[c] : \delta c \rightarrow \lim_{h \rightarrow 0} \frac{\mathcal{I}(c + h\delta c) - \mathcal{I}(c)}{h}.$$

The adjoint state method considers the constrained minimization problem

$$(2.46) \quad \min_c \mathcal{I}(c) \quad \text{subject to (2.16)}.$$

The constraint can be replaced by the variational formulation (2.41) and the associated formulation of the Lagrangian is defined by

$$(2.47) \quad \begin{aligned} \mathcal{L}(c, G, \tilde{\gamma}) = \mathcal{I}(c)(y, z) &+ \int_{\Upsilon} k^2 c^{-2}(x) G(x, y) \tilde{\gamma}(x, y, z) - \nabla_x R(x, y) \cdot \nabla_x \tilde{\gamma}(x, y, z) \, dx \\ &+ \int_{\Gamma_2} ik_0 R(x, y) \tilde{\gamma}(x, y, z) \, d\mu(x). \end{aligned}$$

By letting $G = G_c$ be the solution of the forward problem, and hence $R = R_c$, we can form the Fréchet derivative. For the sake of brevity, we use the following notation

$$(2.48) \quad G' = D_c G_c[c] \delta c,$$

and we omit the variables x, y, z (keeping in mind that G_{obs} depends on (x, z) , G_c and G' on (x, y) , and γ on (x, y, z)).

$$(2.49) \quad \begin{aligned} D_c \mathcal{I}[c] \delta c = \operatorname{Re} (D_c \mathcal{L}(c, G, \tilde{\gamma}) \delta c) \Big|_{G=G_c} \\ = \operatorname{Re} \left(2\overline{S_{\mathcal{U}_0}} \int_{\Sigma} (G' \partial_{\nu_x} G_{obs} - G_{obs} \partial_{\nu_x} G') \, d\mu(x) \right. \\ \left. + \int_{\Upsilon} \left(k^2 c^{-2} G' \tilde{\gamma} - 2k^2 c^{-3} G_c \tilde{\gamma} \delta c - \nabla_x G' \cdot \nabla_x \tilde{\gamma} \right) \, dx \right. \\ \left. + \int_{\Gamma_2} ik_0 G' \tilde{\gamma} \, d\mu(x) \right). \end{aligned}$$

Grouping together all the terms containing G' and replacing it by an arbitrary test function $v \in H_{\Gamma_1}^1(\Upsilon)$, the adjoint state γ is chosen as the solution to

$$(2.50) \quad \begin{aligned} 2\overline{S_{\mathcal{U}_0}} \int_{\Sigma} (v \partial_{\nu_x} G_{obs} - G_{obs} \partial_{\nu_x} v) \, d\mu(x) + \int_{\Upsilon} \left(k^2 c^{-2} v \gamma - \nabla_x v \cdot \nabla_x \gamma \right) \, dx \\ + \int_{\Gamma_2} ik_0 v \gamma \, d\mu(x) = 0. \end{aligned}$$

Note that the first term,

$$(2.51) \quad v \rightarrow 2\overline{S_{\mathcal{U}_0}} \int_{\Sigma} (v \partial_{\nu_x} G_{obs} - G_{obs} \partial_{\nu_x} v) \, d\mu(x),$$

is a bounded linear functional of $H_{\Gamma_1}^1(\Upsilon)$. Hence, by the arguments already mentioned in [3, Proposition 3.1], there exists a unique solution $\gamma \in H_{\Gamma_1}^1(\Upsilon)$ to problem (2.50).

With this choice of adjoint state, (2.49) reduces to

$$(2.52) \quad D_c \mathcal{I}[c] \delta c = \operatorname{Re} \left(\int_{\Upsilon} -2k^2 c^{-3} G_c \gamma \delta c \, dx \right).$$

Reassembling with $(y, z) \in K_1 \times K_1$, we get

$$(2.53) \quad \nabla_c \mathcal{J}(x) = -\operatorname{Re} \left(\int_{K_1 \times K_1} 2k^2 c^{-3}(x) G_c(x, y) \gamma(x, y, z) \, dy \, dz \right).$$

Note that G_c is independent of z , hence, posing

$$(2.54) \quad \widehat{\gamma}(x, y) = \int_{K_1} \gamma(x, y, z) dz,$$

we have that $\widehat{\gamma}$ verifies, for every $v \in H_{\Gamma_1}^1(\Upsilon)$,

$$(2.55) \quad \begin{aligned} & 2 \int_{K_1} \overline{S_{U_0}} \int_{\Sigma} (v \partial_{\nu_x} G_{obs} - G_{obs} \partial_{\nu_x} v) d\mu(x) dz \\ & + \int_{\Upsilon} \left(k^2 c^{-2} v \widehat{\gamma} - \nabla_x v \cdot \nabla_x \widehat{\gamma} \right) dx + \int_{\Gamma_2} i k_0 v \widehat{\gamma} d\mu(x) = 0. \end{aligned}$$

3 Computational experiments

For the numerical experiments we consider a three-dimensional model (courtesy Statoil), which is illustrated in Figure 1. To have a clear visualization of the wave speed structures, we show horizontal and vertical sections at $z = 800$ m and $y = 1.125$ km respectively. The model is of size $2.55 \times 1.45 \times 1.22$ km with variations of wave speed from 1500 to 5200 m s^{-1} . We assume that the density is constant with $\rho = 1000 \text{ kg m}^{-3}$.

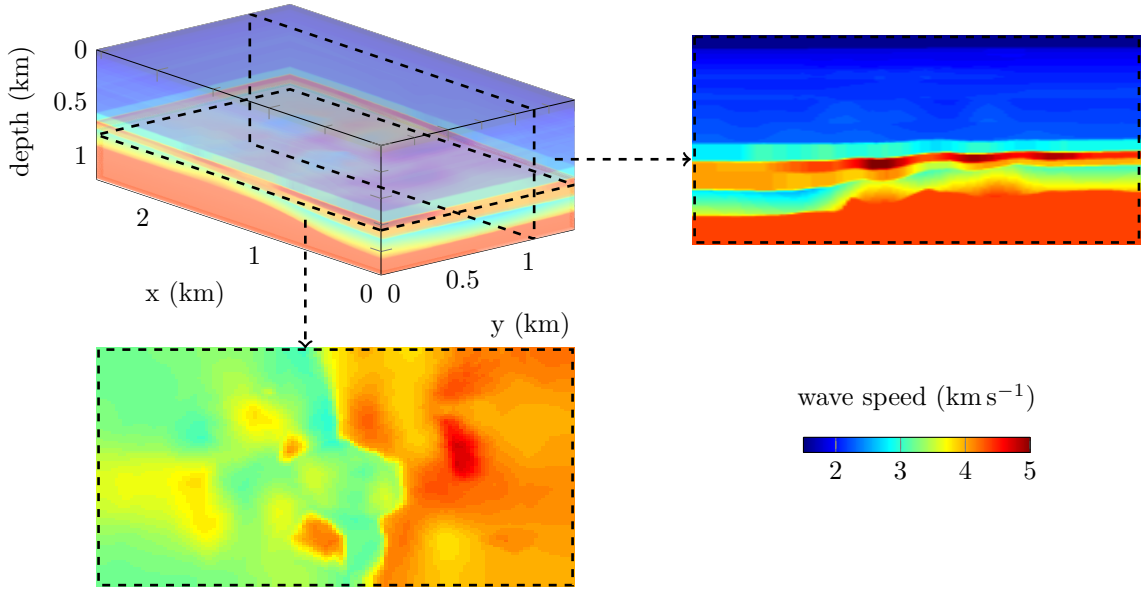


Figure 1: Three-dimensional representation, horizontal section at 800 m depth and vertical section at $y = 1.125$ km of the reference wave speed. It is represented with 1 527 168 nodal values.

The seismic acquisition consists of 160 sources and 1376 receivers, that is, dual sensors recording the Cauchy data probed by the sources. The receivers are positioned on a regular 43 (along the x -axis) by 32 (along the y -axis) grid at a fixed depth below the sources lattice. The configuration is illustrated in Figure 2. We consider two situations for the discretized sources map: the sources are first contained in a solid region, in accordance with the above analysis (see Figure 2(b)). Then, they are restricted on a two-dimensional lattice (see Figure 2(c)). The first approach, less common in seismic applications, is yet possible with recent acquisition technique described in Footnote 1, for which the depth of the sources can vary. Following the situation prescribed in Subsection 2.3, we assume that the uppermost part of the model (which is water), in which the Cauchy data are obtained, is known prior to the reconstruction. We impose a free surface, Dirichlet boundary condition on the top part, Γ_1 , of $\partial\Upsilon$ and absorbing boundary conditions on $\Gamma_2 = \partial\Upsilon \setminus \overline{\Gamma_1}$, by taking $k_0 = \omega c_0^{-1}$ in the third equation of (2.16), following Engquist and Majda [16].

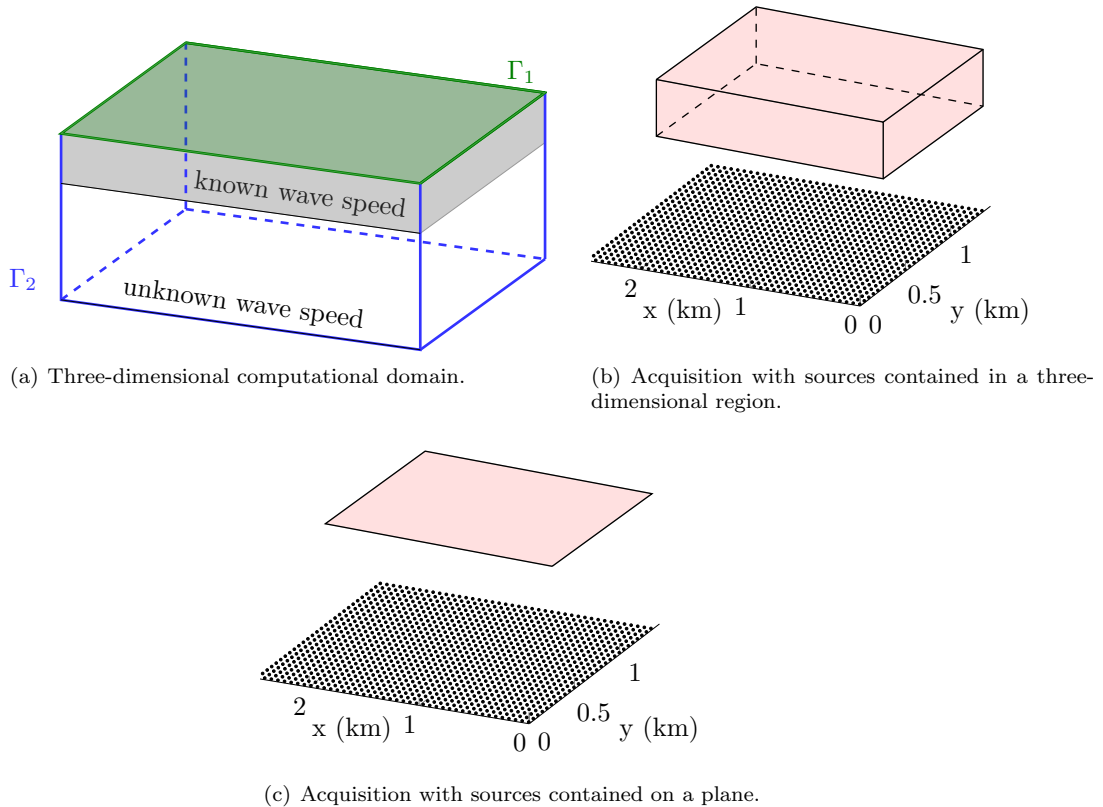


Figure 2: Illustration of the configuration. (a) We apply a Dirichlet boundary on the upper surface Γ_1 (in green) and absorbing boundary conditions on $\Gamma_2 = \partial\Upsilon \setminus \bar{\Gamma}_1$ (indicated in blue). (b)–(c) The sources that probe the Cauchy data lie in between the receivers and the free surface. Sources are positioned in a three or two-dimensional region (in red). The position of the receivers (black dots) remains fixed. Both receivers and sources lie in the area of known velocity.

Synthetic dual-sensor data are generated in the time-domain using a Discontinuous Galerkin finite element method². The original data for a single centered source are presented in Figures 3 and 4 for the pressure and vertical velocity respectively. In the figures, we can observe the difference of scale in the amplitudes between the pressure and the vertical velocity.

We subject the (time-domain) data to a Fourier transform to obtain time-harmonic data. We select frequencies from 3 to 15 Hz, using a 1 Hz increment. These are the data that we will use for our reconstruction algorithm and underlying iterative minimization of the misfit functional (2.27). We simulate time-harmonic data using a Continuous Galerkin finite element method. We use an approach and implementation similar to the one discussed in Shi *et al.* [28]. The relevant system of equations are solved with the direct structured solver MUMPS, [4]. The numerical discretization introduces a tetrahedral representation of the model, which we illustrate in Figure 5.

For the construction of the hierarchy of stable subspaces, the domain partition determining the piecewise linear representation of the wave speed is typically significantly coarser than the tetrahedral mesh. Hence, we define every subdomain, D_j , as the union of mesh elements, K_i , according to

$$(3.1) \quad D_j = \bigcup_{i=1}^{N_j} K_i,$$

where N_j denotes the number of mesh elements in D_j .

²The code that was used, here, can be found at <https://team.inria.fr/magique3d/software/hou10ni/>.

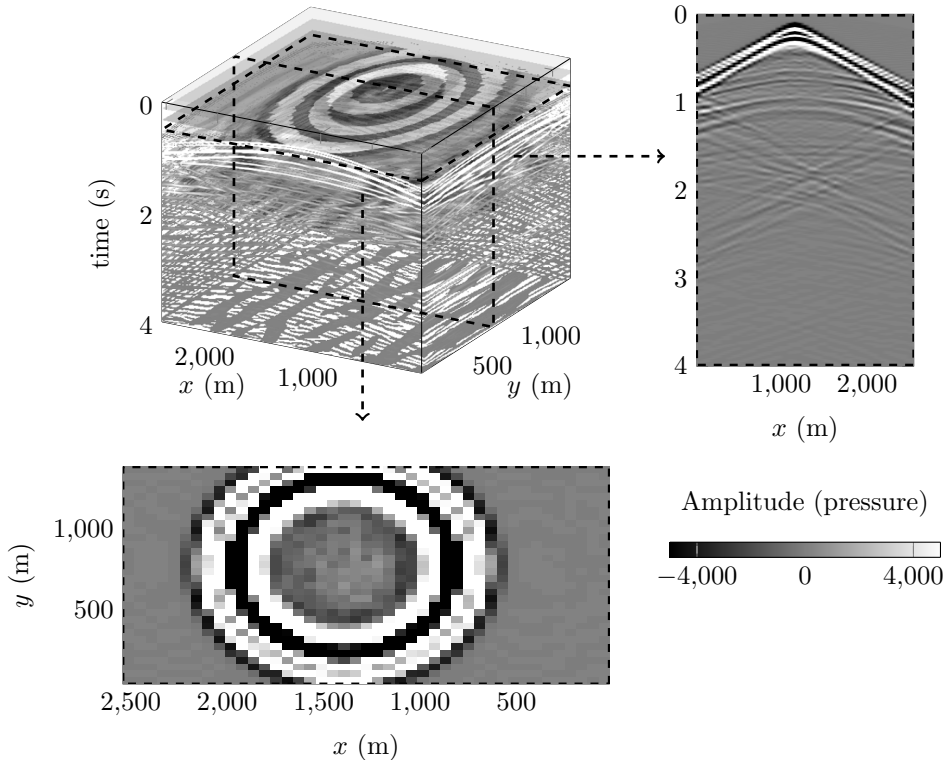


Figure 3: Three-dimensional time-domain pressure trace for a centrally located source. Sections at fixed time $t = 0.5$ s and for a fixed line of receivers positioned in $y = 695$ m are respectively given at the bottom and right of the 3D visualization. The x and y axis correspond with the receivers map (*i.e.*, every 60 m for x and 45 m for y).

Inherent model error is introduced from those two levels of representation. Because we do not know the subsurface geometry a priori, the piecewise linear partition relies on the gradient of the misfit functional. Naturally, the more subdomains are taken, the more accurate can the representation be.

We consider two scenarios for the reconstruction. Firstly, we proceed using single-frequency, 10 Hz data and a fixed domain partition. Exploiting the Lipschitz stability result obtained in Theorem 2 above, the Landweber iteration [15] provides a convergence analysis. The initial model needs to be within the radius of convergence. Secondly, we invoke a multi-level algorithm [15] with frequency progression in concert with scale progression. The progression is controlled by the stability constants associated with the hierarchy of stable subspaces. This enlarges the radius of convergence to a degree that, essentially, minimal prior knowledge is required.

3.1 Single-frequency data

From the Cauchy data at 10Hz, we carry out a reconstruction of the reference model starting from the smooth model depicted Figure 6. We encode the principal variation and appropriate order of magnitude of the wave speed in the initial model.

For the reconstruction, here, we use a conjugate gradient method. The model is partitioned in 1089 subdomains where piecewise linear functions are used to define the wave speed. This leads to a total number of unknowns of $4 \times 1089 = 4356$ (while the reference medium has 1 527 168 nodal values, see Figure 1). The key, here, is the low-dimensional subspace used for regularization. The partition is adapted to the gradient computation via segmentation. We carry out 175 iterations. In Figure 7(a), we show the reconstruction when the sources are positioned in a volume above the receivers (see Figure 2(b)); in Figure 7(b), we show the reconstruction when the sources are restricted on a two-dimensional plane (see Figure 2(c)).

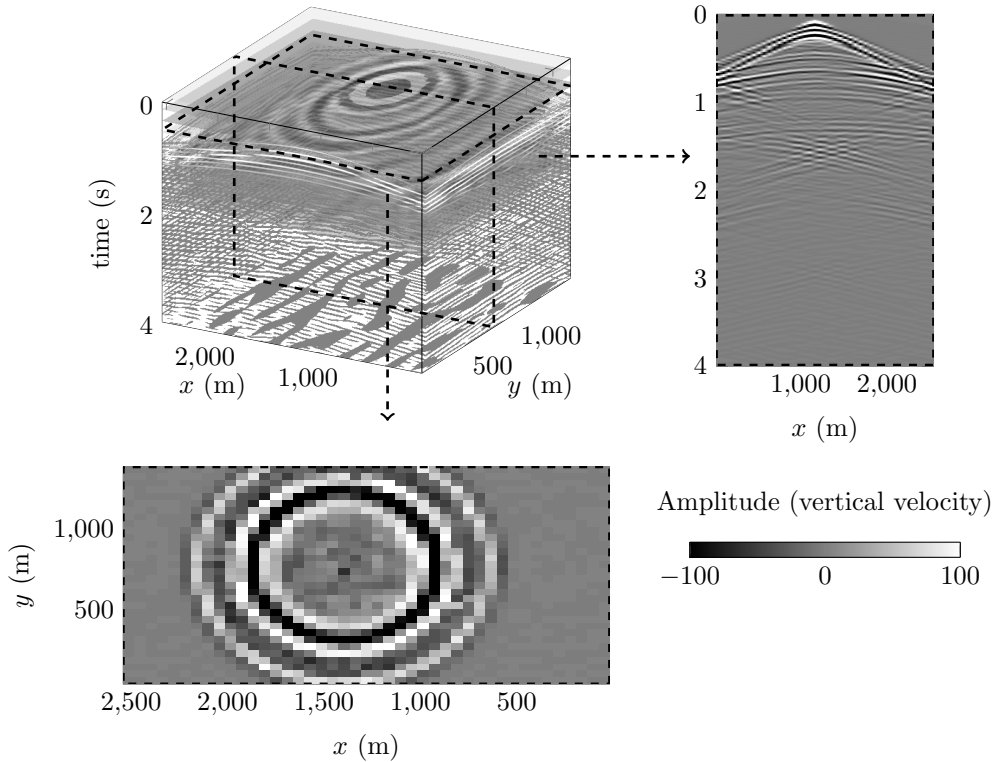


Figure 4: Three-dimensional time-domain vertical velocity trace for a centrally located source. Sections at fixed time $t = 0.5$ s and for a fixed line of receivers positioned in $y = 695$ m are respectively given at the bottom and right of the 3D visualization. The x and y axis correspond with the receivers map (*i.e.*, every 60 m for x and 45 m for y).

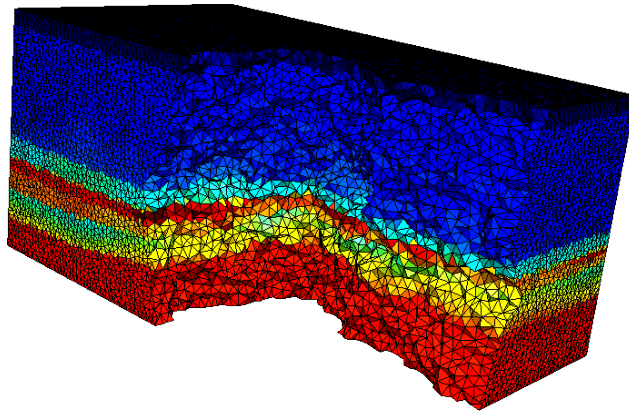


Figure 5: Illustration of the unstructured tetrahedral mesh decomposition of the model, using 433 979 tetrahedra.

The two acquisitions provide accurate recoveries of the subsurface, with some improvement when the sources are positioned in a volume: the width of the increased velocity layer and the deepest values of the wave speed are better retrieved with this type of acquisition. However, the reconstruction from sources limited on a plane is very close. In the subspace, we have drastically reduced the number of unknowns in the representation as compared with the original representation, namely to 0.3%. Nonetheless, the reconstruction captures the main features of the model, including the alternation of high and low values in the vertical direction and the resolution remains reasonable.

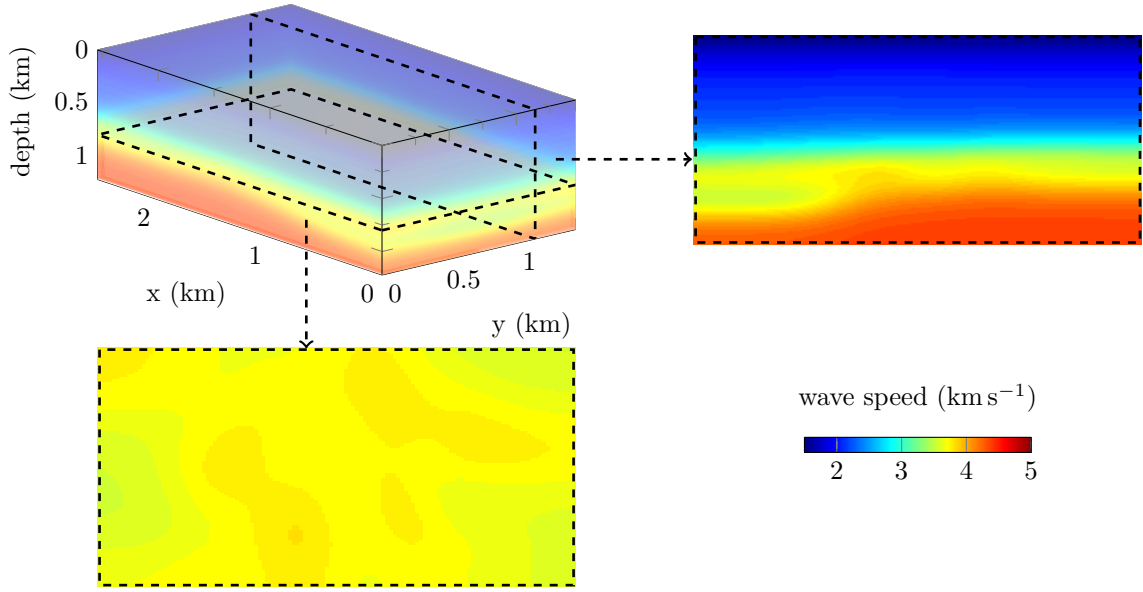
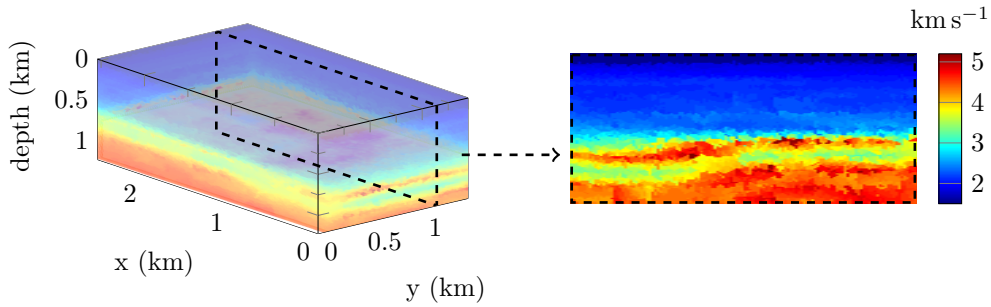
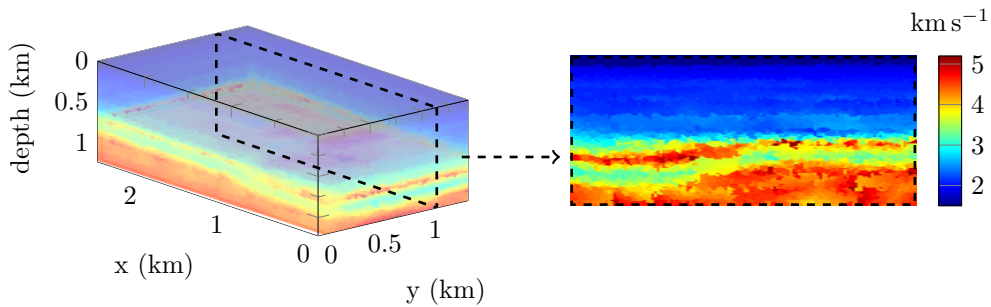


Figure 6: Three-dimensional representation, horizontal section at 800 m depth and vertical section at $y = 1.125$ km of the initial wave speed model.



(a) Reconstruction where the sources in the acquisition are positioned in a three-dimensional area (see Figure 2(b))



(b) Reconstruction where the sources in the acquisition are limited on a plane (see Figure 2(c))

Figure 7: Three-dimensional representation and vertical section at $y = 1.125$ km of the reconstruction from 10 Hz Cauchy data after 175 iterations. The partition consists of $N = 1089$ subdomains, leading to a total number of unknowns of $4 \times 1089 = 4356$. The initial model is shown in Figure 6.

Remark 2 (Improved visualization with Gaussian filtering). *The visualization of the reconstruction may suffer from the tetrahedral mesh employed for the numerical discretization. It is simple to improve the visualization by applying a smoothing filter onto the image. This can be done, for example, with the `imgaussfilt` function of MATLAB, which applies a Gaussian smoothing filter. In Figure 8, we show the resulting image when applied onto the reconstruction of Figure 7(b). It allows a better identification of the recovered structures. Note that this procedure is done a-posteriori, independently of the reconstruction algorithm, and is effortless.*

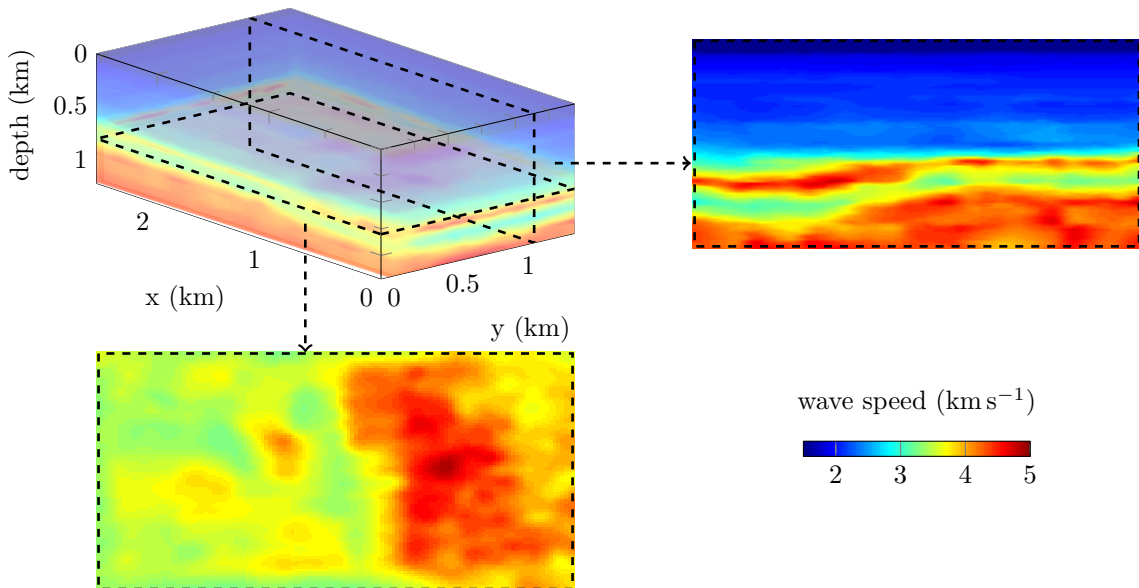


Figure 8: Gaussian filtering of the reconstruction obtained from 10Hz Cauchy data (Figure 7(b)), three-dimensional representation, horizontal section at 800 m depth and vertical section at $y = 1.125$ km.

In the following experiments, we only consider the case where sources are restricted on a plane, following the acquisition illustrated Figure 2(c), for simplicity.

3.2 Single-frequency data, depth varying initial model

We repeat the experiment carried out in the previous subsection (with the two-dimensional sources lattice), but with a simplified initial model, see Figure 9. That is, here, the initial model only contains an indication of the average variation of wave speed in depth. The idea behind this experiment is to test the radius of convergence on the one hand, and the closeness of the true model and the best projection onto a low-dimensional stable subspace on the other hand.

In Figures 10 and 11, we present the result after 175 iterations using 10 Hz Cauchy data. As in the first experiment, we have 1089 subdomains in the partition and piecewise linear representations. Despite the lack of initial information we still retrieve the main features and appropriate contrasts in the wave speed. However, we lost accuracy as compared with the previous example (especially on the side), but the deep layer of low wave speed is well identified nonetheless.

Figures 12 and 13 compare the observed, initial and reconstruction data, using the full receivers map associated with a centrally located source. We see that the data from the recovered velocity provide a pattern that is similar to the Fourier transform of the time-domain observations.

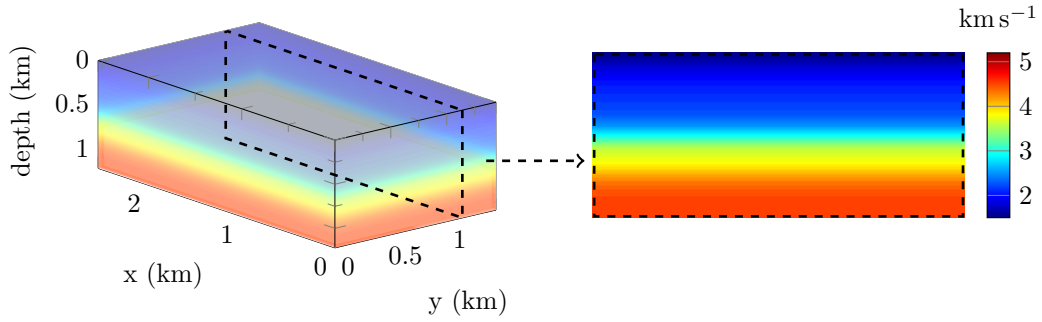


Figure 9: Three-dimensional representation and vertical section at $y = 1.125$ km of the initial model, which varies in depth only.

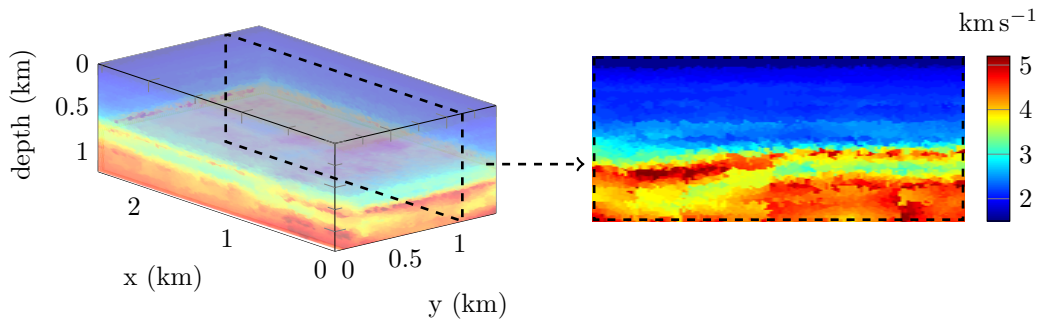


Figure 10: Three-dimensional representation and vertical section at $y = 1.125$ km of the reconstruction from 10 Hz Cauchy data after 175 iterations. The partition consists of $N = 1089$ subdomains, leading to a total number of unknowns of $4 \times 1089 = 4356$. The initial model varies in depth only and is shown in Figure 9.

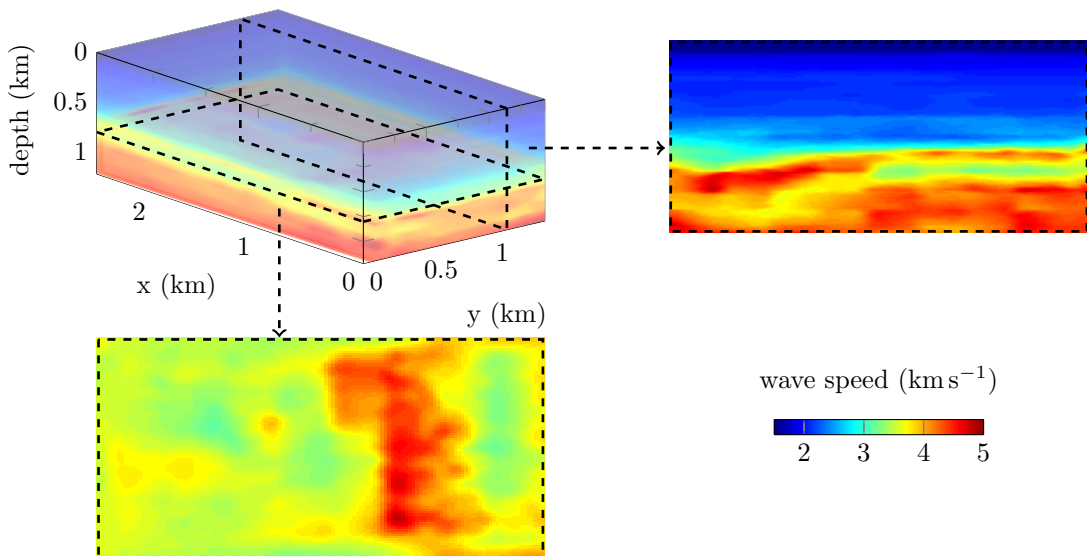
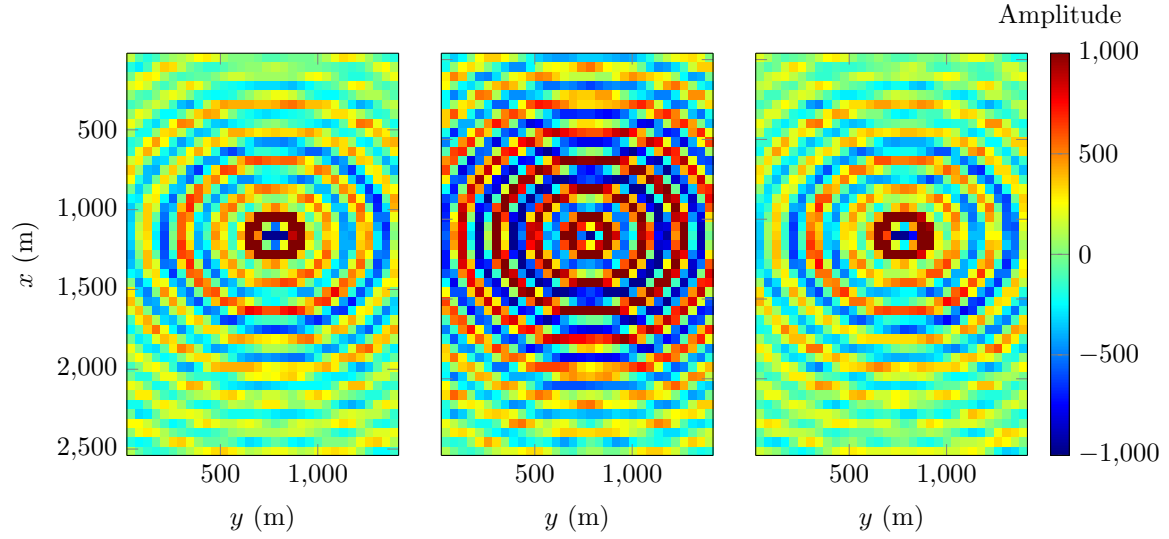
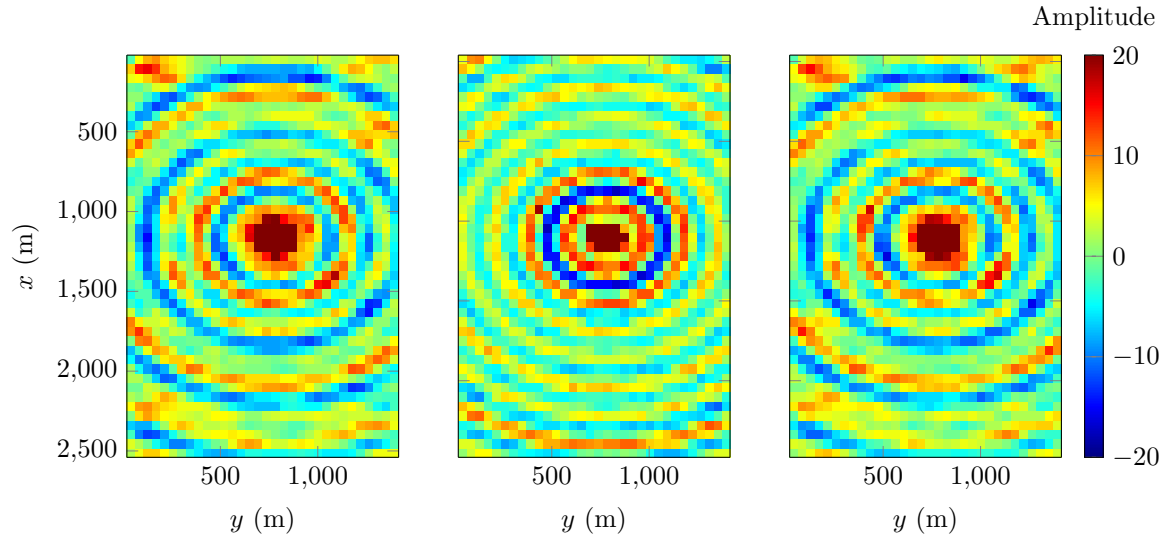


Figure 11: Gaussian filtering (see Remark 2) of the reconstruction (Figure 10) obtained from 10Hz Cauchy data starting with the initial model that varies in depth only (Figure 9). Three-dimensional representation, horizontal section at 800 m depth and vertical section at $y = 1.125$ km.



(a) Fourier transform of the time-domain observation. (b) Simulated data using the initial model of Figure 9. (c) Simulated data from the reconstructed model Figure 10.

Figure 12: Comparison of the 10 Hz frequency pressure data captured at the receivers location for a centrally located source.



(a) Fourier transform of the time-domain observation. (b) Simulated data using the initial model of Figure 9. (c) Simulated data from the reconstructed model Figure 10.

Figure 13: Comparison of the 10 Hz frequency vertical velocity data captured at the receivers location for a centrally located source.

3.3 Multi-frequency data and multi-level reconstruction

We now carry out a multi-level reconstruction from multi-frequency data, from 3 to 15 Hz. Increasing the frequency range allows us to start with less prior information for the initial model. As anticipated, the low frequencies play a critical role here. Our initial model is, again, varying in depth only but with a much smaller range than in the previous experiment; see Figure 14.

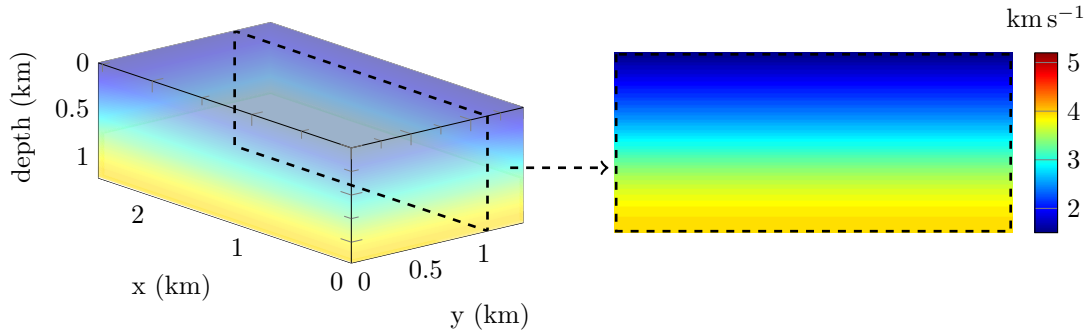


Figure 14: Three-dimensional representation, vertical section at $y = 1.125$ km of the initial wave speed model used for multi-level, multi-frequency reconstruction.

The multi-level reconstruction associates frequency with scale progression. For this test, we perform 20 iterations per frequency, from 3 to 15 Hz. The scale progression is motivated by the conditional stability estimates. In the absence of a quantitative estimate, we use computations and follow the progression in Table 1.

Frequency	Number of subdomains	Number of unknowns
3 Hz	150	600
4 Hz	210	840
5 Hz	441	1764
6 Hz	880	3520
7 Hz	1690	6760
{8, 9, 10, 12, 14, 15} Hz	13 000	52 000

Table 1: Coupling frequency and scale in our multi-level reconstruction experiment. 20 iterations are processed per frequency.

The final reconstruction after the 15 Hz iterations is presented in Figures 15 and 16. Despite the lack of initial information, the multi-level procedure using the Cauchy data recovers the subsurface area with significant accuracy and visible improvement compared to the use of single frequency data.

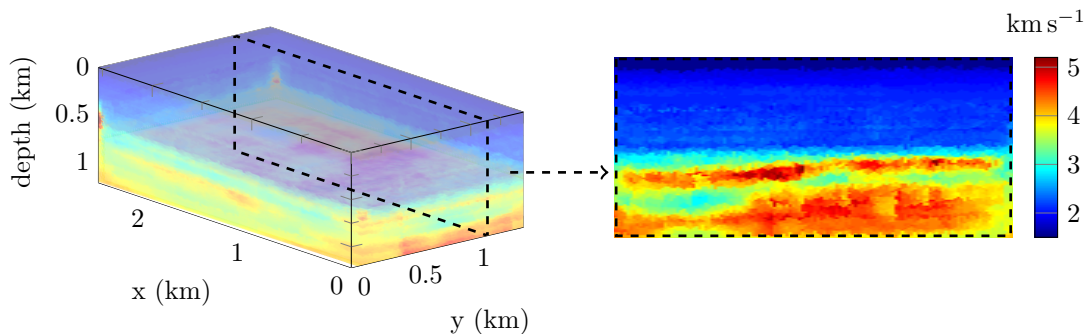


Figure 15: Three-dimensional representation and vertical section at $y = 1.125$ km of the final reconstruction using multi-frequency Cauchy data.

In Figures 17 and 18, we compare the observed, initial and recovered data at the receivers location. The selected frequency content is 12 Hz, for a centrally located source. The reconstruction approaches the Fourier transform of the time-domain observations accurately, both for the pressure and vertical

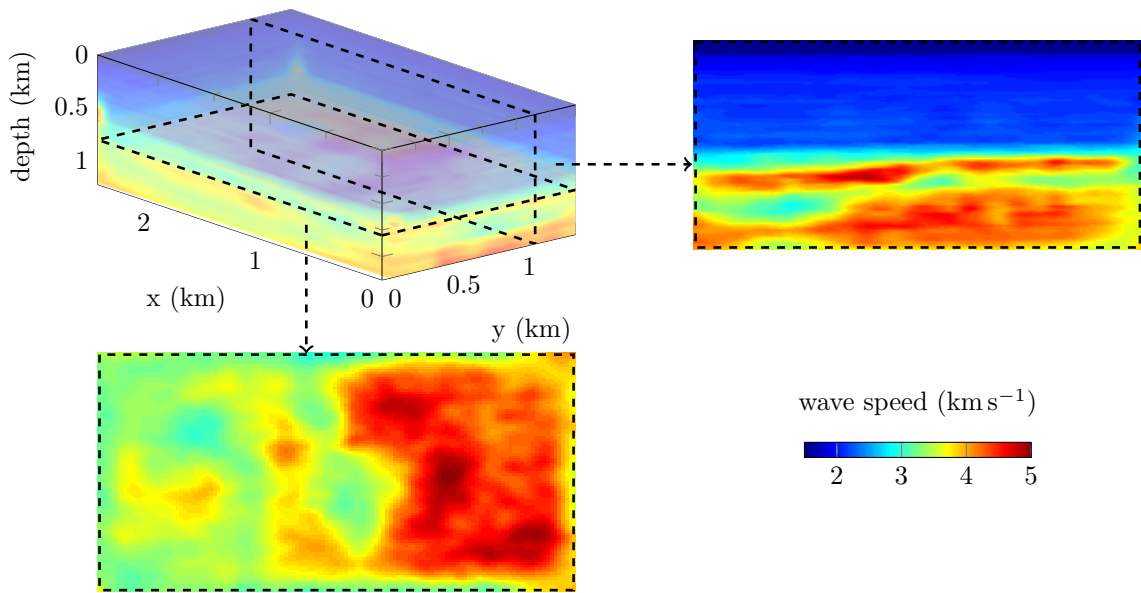
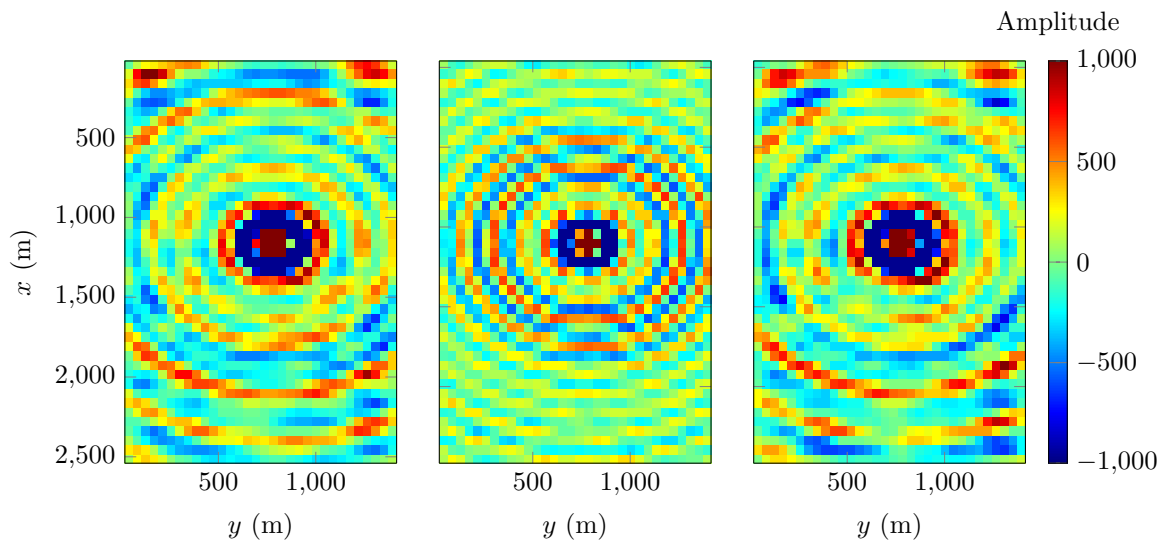


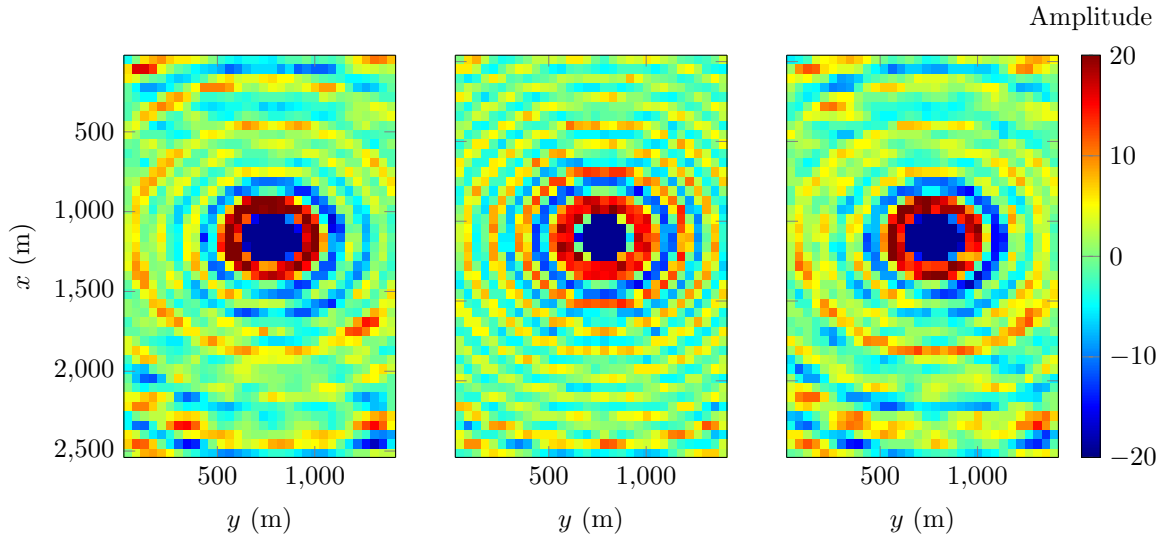
Figure 16: Gaussian filtering (see Remark 2) of the reconstruction (Figure 15) obtained using multi-frequency Cauchy data. Three-dimensional representation, horizontal section at 800 m depth and vertical section at $y = 1.125$ km.

velocity data.



(a) Fourier transform of the time-domain observation. (b) Simulated data using the initial model of Figure 14. (c) Simulated data from the reconstructed model Figure 15.

Figure 17: Comparison of the 12 Hz frequency pressure data captured at the receivers location for a centrally located source.



(a) Fourier transform of the time-domain observation.

(b) Simulated data using the initial model of Figure 14.

(c) Simulated data from the reconstructed model Figure 15.

Figure 18: Comparison of the 12 Hz frequency vertical velocity data captured at the receivers location for a centrally located source.

4 Perspectives on independent locations of sources in the discretized settings

The misfit functional (2.27) defined for the Cauchy data has an interesting feature, because of the intuitive differentiation between acquisition sets for the observations and simulations. It is materialized by the double integral over $K_1 \times K_1$. The perspective is here to separate in, say, $K_2 \times K_1$.

In the usual context of minimization involving the direct difference between observations and simulations, such as the standard least squares, the setup for simulation is imposed by the field acquisition (source position and wavelet). Consequently, absence of knowledge leads to the failure of the algorithm. Here, providing this new misfit functional, we expect our iterative minimization algorithm to be free of those considerations, introducing extreme flexibility for the setup, where only the position of the receivers is required.

In order to illustrate the potential of the method, we reproduce the experiment designed in Subsection 3.3 but differentiating the simulation set from the observation set. Namely we halve the number of sources compared to the observation set, their positions are changed and we choose a different source wavelet, see Table 2.

	Setup for measurements	Setup for simulations
Number of sources	160	80
Depth of the sources	100 m	80 m

Table 2: Comparison of acquisition setups employed for the observations and simulations. The source wavelet also differs.

We conduct the iterative minimization similarly to the previous example, following the progression in frequency and scale prescribed in Table 1. The reconstruction after the 15 Hz iterations is shown Figures 19 and 20.

The reconstruction captures the main variations and accurately recovers the wave speed. We have halved the number of sources in the simulation compared to the observation, reducing the numerical cost accordingly, yet we make full use of the observed data from the benefit of our misfit functional

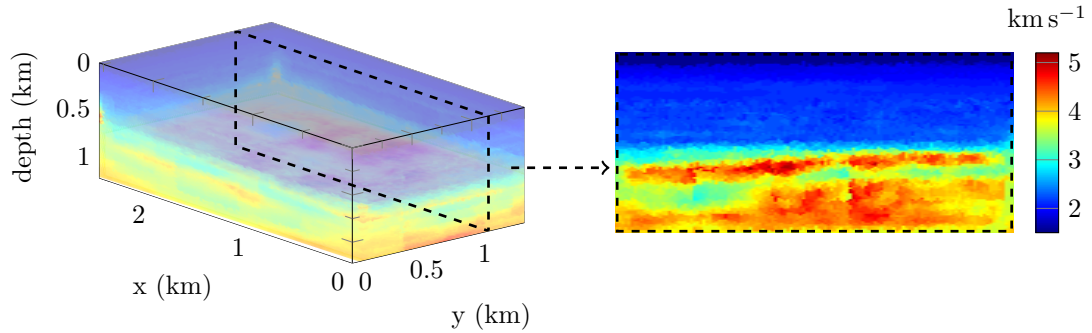


Figure 19: Three-dimensional representation and vertical section at $y = 1.125$ km of the final reconstruction using multi-frequency Cauchy data where the simulation setup differs from the original measurement acquisition, see Table 2.

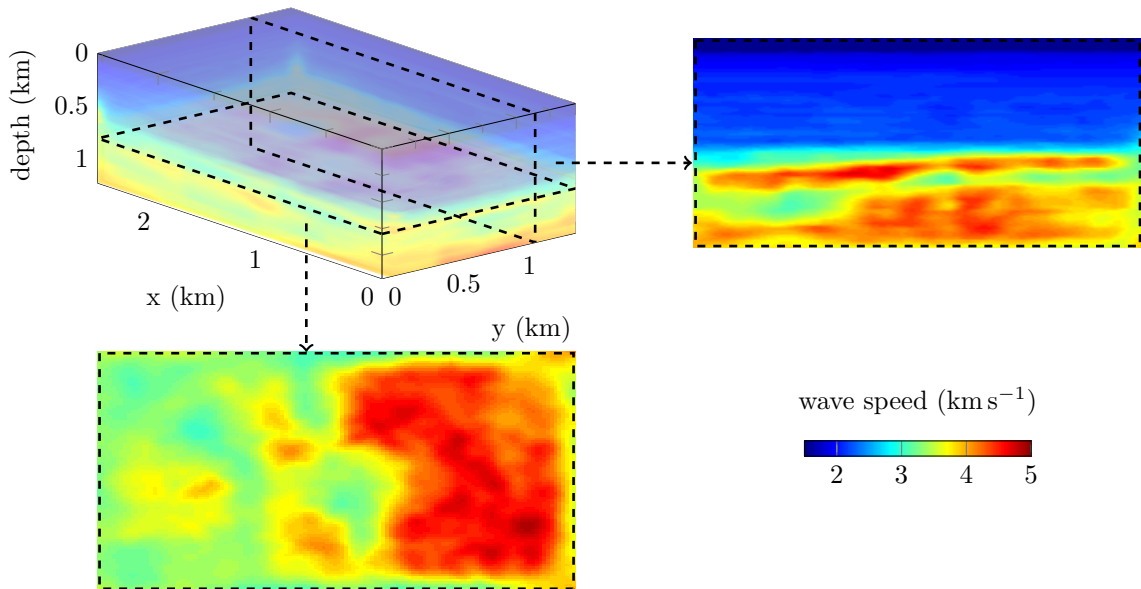


Figure 20: Gaussian filtering (see Remark 2) of the reconstruction (Figure 19) obtained using multi-frequency Cauchy data and where the setup for simulation differs from the original measurement acquisition. Three-dimensional representation, horizontal section at 800 m depth and vertical section at $y = 1.125$ km.

defined for Cauchy data. Furthermore we do need to know the position of the sources employed for observation, nor the source wavelet. Eventually we even observe similar accuracy as in the experiment of Subsection 3.3 where sources collocation is considered.

The perspective of differentiating the observations and simulations acquisition sets is a promising application, and appears consistent with the results of this preliminary experiment. It would allow less prior on the observational environment, increasing the robustness of the procedure, without impacting the resolution of the reconstruction.

5 Acknowledgment

The research of G. Alessandrini and E. Sincich for the preparation of this paper has been supported by FRA 2016 “Problemi inversi, dalla stabilità alla ricostruzione”, funded by Università degli Studi di Trieste. Maarten V. de Hoop acknowledges the Simons Foundation under the MATH+X program for

financial support. He was also partially supported by NSF under grant DMS–1559587. R. Gaburro wishes to acknowledge the support of MACSI, the Mathematics Applications Consortium for Science and Industry (www.macsi.ul.ie), funded by the Science Foundation Ireland Investigator Award 12/IA/1683. E. Sincich has also been supported by Gruppo Nazionale per l’Analisi Matematica, la Probabilità e le loro Applicazioni (GNAMPA) by the grant “Analisi di problemi inversi: stabilità e ricostruzione”.

References

- [1] R. A. Adams and J. J. F. Fournier, Sobolev Spaces, Elsevier Science, 2003.
- [2] V. Akcelik, G. Biros and O. Ghattas, Parallel Multiscale Gauss-Newton-Krylov Methods for Inverse Wave Propagation, Supercomputing, ACM/IEEE 2002 Conference (2002), 41pp.
- [3] G. Alessandrini, M.V. de Hoop, R. Gaburro and E. Sincich, Lipschitz stability for a piecewise linear Schrödinger potential from local Cauchy data, arXiv preprint arXiv:1702.04222 (2017).
- [4] P. R. Amestoy, A. Guermouche, J.-Y. L’Excellent and S. Pralet, Hybrid scheduling for the parallel solution of linear systems, Parallel computing, **32** (2) (2006), 136–156.
- [5] J. B. Bednar, C. Shin and S. Pyun, Comparison of waveform inversion, part 2: phase approach, Geophysical Prospecting **55** (4) (2007), 465–475.
- [6] E. Beretta, M. De Hoop and L. Qiu, Lipschitz stability of an inverse boundary value problem for a Schrödinger type equation, SIAM J. Math. Anal. **45** (2) (2013), 679–699.
- [7] E. Bozdağ, J. Trampert and J. Tromp, Misfit functions for full waveform inversion based on instantaneous phase and envelope measurements Geophysical Journal International **85** (2) (2011), 845–870.
- [8] R. Brossier, S. Operto and J. Virieux, Robust elastic frequency-domain full-waveform inversion using the $L1$ norm Geophysical Research Letters **36** (20) (2009).
- [9] R. Brossier, S. Operto and J. Virieux, Which data residual norm for robust elastic frequency-domain full waveform inversion? Geophysics **75** (3) (2010), R37–R46.
- [10] C. Bunks, Fatimetou M. Saleck, S. Zaleski and G. Chavent, Multiscale seismic waveform inversion, Geophysics **60** (5) (1995), 1457–1473.
- [11] F. Cakoni and D. L. Colton, A qualitative approach to inverse scattering theory, Springer (2014).
- [12] D. Carlson, W. Söllner, H. Tabti, E. Brox and M. Widmaier, Increased resolution of seismic data from a dual-sensor streamer cable, SEG Technical Program Expanded Abstracts 2007, 994–998, Society of Exploration Geophysicists (2007).
- [13] C. I. Cârstea, N. Honda and G. Nakamura, Uniqueness in the inverse boundary value problem for piecewise homogeneous anisotropic elasticity, arXiv preprint arXiv:1611.03930v2 (2016).
- [14] G. Chavent, Identification of functional parameters in partial differential equations, Identification of Parameters in Distributed Systems (1974).
- [15] M. De Hoop, L. Qiu and O. Scherzer, Local analysis of inverse problems: Hölder stability and iterative reconstruction, Inverse Problems **28** (4) (2012): 045001.
- [16] B. Engquist and A. Majda, Absorbing boundary conditions for numerical simulation of waves, Proceedings of the National Academy of Sciences **74** (5) (1977), 1765–1766
- [17] B. L. N. Kennett, M. S. Sambridge and P. R. Williamson, Subspace methods for large inverse problems with multiple parameter classes, Geophysical Journal International **94** (1988), 237–247.

- [18] P. Lailly, The seismic inverse problem as a sequence of before stack migrations, Conference on Inverse Scattering: Theory and Application, Society for Industrial and Applied Mathematics, 206-220, J. B. Bednar, (1983).
- [19] J. L. Lions and S. K. Mitter, Optimal control of systems governed by partial differential equations, Springer Berlin (1971).
- [20] Y. Lin, A. Abubakar and T. M. Habashy, Seismic full-waveform inversion using truncated wavelet representations, in SEG Technical Program Expanded Abstracts 2012, chapter 486 (2012), 1-6.
- [21] I. Loris, H. Douma, G. Nolet, I. Daubechies and C. Regone, Nonlinear regularization techniques for seismic tomography, Journal of Computational Physics **229** (2010), 890-905.
- [22] I. Loris, G. Nolet, I. Daubechies and F.A. Dahlen, Tomographic inversion using L1-norm regularization of wavelet coefficients, Geophysical Journal International **170** (2007), 359-370.
- [23] G. S. Pan, R. A. Phinney and R. I. Odom, Full-waveform inversion of plane-wave seismograms in stratified acoustic media; theory and feasibility, Geophysics **53** (1) (1988), 21-31.
- [24] R.-E. Plessix, A review of the adjoint-state method for computing the gradient of a functional with geophysical applications, Geophysical Journal International **167** (2) (2006), 495-503.
- [25] R. G. Pratt, Z.-M. Song, P. Williamson and M. Warner, Two-dimensional velocity models from wide-angle seismic data by wavefield inversion, Geophysical Journal International **124** (1996), 323-340.
- [26] R. G. Pratt and M. H. Worthington, Inverse theory applied to multi-source cross-hole tomography. Part 1: Acoustic wave-equation method, Geophysical Prospecting **38** (1990), 287-310.
- [27] G. Rønholt, J. E. Lie, O. Korsmo, B. Danielsen, S. Brandsberg-Dah, S. Brown, N. Chemingui, A Valenciano Mavilio, D. Whitmore and R. D. Martinez, Broadband velocity model building and imaging using reflections, refractions and multiples from dual-sensor streamer data, 14th International Congress of the Brazilian Geophysical Society & EXPOGEF, Rio de Janeiro, Brazil, 3-6 August 2015, 1006-1009, Brazilian Geophysical Society (2015).
- [28] J. Shi, M.V. de Hoop, E. Beretta, E. Francini and S. Vessella, Multi-parameter iterative reconstruction with the Neumann-to-Dirichlet map as the data, preprint (2017).
- [29] S. Pyun, C. Shin, and J. B. Bednar, Comparison of waveform inversion, part 3: amplitude approach, Geophysical Prospecting, **55** (4) (2007), 477-485.
- [30] C. Shin, S. Pyun, and J. B. Bednar, Comparison of waveform inversion, part 1: conventional wavefield vs logarithmic wavefield, Geophysical Prospecting, **55** (4) (2007), 449-464.
- [31] A. Tarantola, Inversion of seismic reflection data in the acoustic approximation, Geophysics **49** (1984), 1259-1266.
- [32] A. Tarantola, Inversion of travel times and seismic waveforms, Seismic tomography, 135 - 157, Springer, (1987).
- [33] R. Tenghamn, S. Vaage and C. Borresen, A dual-sensor towed marine streamer: Its viable implementation and initial results, SEG Technical Program Expanded Abstracts 2007, 989-993, Society of Exploration Geophysicists (2007).
- [34] N. D. Whitmore, A. A. Valenciano, W. Sollner and S. Lu, Imaging of primaries and multiples using a dual-sensor towed streamer, SEG Technical Program Expanded Abstracts 2010, 3187-3192, Society of Exploration Geophysicists (2010).
- [35] R.-S. Wu, J. Luo and B. Wu, Seismic envelope inversion and modulation signal model, Geophysics **79** (3) (2014), WA13-WA24.

- [36] Y. O. Yuan and F. J. Simons, Multiscale adjoint waveform-difference tomography using wavelets, *Geophysics* **79** (3), Society of Exploration Geophysicists (2014), WA79–WA95.
- [37] Y. O. Yuan, F. J. Simons and E. Bozdağ, Multiscale adjoint waveform tomography for surface and body waves, *Geophysics* **80** (5), Society of Exploration Geophysicists (2015), R281–R302.